MDPI

Article

Monolithic PneuNets Soft Actuators for Robotic Rehabilitation: Methodologies for Design, Production and Characterization

Monica Tiboni * and **Davide Loda**

Department of Mechanical and Industrial Engineering, University of Brescia, Via Branze, 38, 25123 Brescia, Italy; d.loda007@studenti.unibs.it

* Correspondence: monica.tiboni@unibs.it; Tel.: +39-3316-133-392

Abstract: Soft-robotics for biomedical applications, such as rehabilitation robots, is a field of intense research activity. Different actuation solutions have been proposed in the last decades, involving study and development of soft actuators of different types and materials. The purpose of the paper is to present procedures for an optimized design, and for easy and low cost production and characterization of monolithic PneuNets soft-actuators. An innovative design approach has been developed. The parameterization of the geometry, combined with FEM simulations is the basis for an optimized design of the actuator, as a function of the obtained bending and of the generated forces. Simple and cheap characterization setup and procedures have been identified for the actuator characterization and for simulation results validation. An easy and low-cost fabrication method based on lost wax core obtained through a silicone based mold has been developed for a monolithic PneuNets soft-actuator. The proposed solution performs well in bending, without the need for a strain limiting layer. Experimental results validated simulations, confirming the feasibility of adopting an optimized simulation-based design approach.

Keywords: soft actuators; pneunets; robotic rehabilitation; monolithic structure; FEM analysis; experimental characterization

1. Introduction

Loss of hand movement control plays a major role in assessing an individual's quality of life: indeed the effectiveness of basic and instrumental tasks of daily life can be compromised following a neurological damage or an accident [1]. In recent years, the scientific community has increasingly shown interest in the application of robotic solutions for rehabilitative practices [2,3]. Since these practices are costly in terms of time, labor and based on repetitive movements [4], robotic systems can be exploited in order to carry out autonomous or supervised rehabilitative routines [5–9]. Results-wise, data concerning the effect of robots usage in hand rehabilitation can be gathered from numerous researches showing promising outcomes [10–14], in particular on stroke patients [15–18].

Soft robotics is a growing field that involves the use of compliant materials (such as rubber and silicone) and mechanisms to create robots that are safer, more adaptable, less expensive, and more effective at interacting with the human body than traditional rigid robots [4,19,20]. A classical approach often adopted in rehabilitation robotics is to build rigid exoskeletons with a fixed number of degree of freedom [14,21,22]. These structures are generally robust and capable of driving considerable amount of forces, but some problems may arise when they are applied to human joints. Misalignment between human and robot joint axis may in fact be cause of user's discomfort and therefore design and production must be carried out with great care. Moreover, actuation often requires motors, transmission gear trains, linkages or tendons at the possible cost of making the final structure bulky and complex.

The use of a soft actuator can ultimately make the rehabilitation process more accessible both from the perspective of trained personnel and patients than the use of a rigid

exoskeleton. In addition, through integration with sensors or vision systems, practices such as mirror therapy [23] can be implemented, which could be performed by the patient himself after appropriate training by experienced technicians.

Researchers have evaluated several different actuation techniques for soft robots over time and some of the most common ones include: pneumatics, hydraulics, electric motors, actuators based on shape memory alloys, and electro-magnetic soft actuators, or more in general soft-actuators. Pneumatic [4] and hydraulic [24] based actuators share a common physical working principle: the application of an input force, provided by compressed air or other fluids, results in a deformation of their structures exerting forces and/or moments on the external environment. Shape memory alloys (or SMAs) are materials that deform when exposed to heat: SMAs systems can be used in order to realize wide varieties of configurations due to their flexibility, but actuation is generally slow in time and complex to control [25]. Electric motors driven systems are often based on flexible tendon connected to a linear [26] or rotary motor [27]: this choice allows precise and controllable movements. Electromagnetic soft actuators embed in their structure magnetizable elements that can either attract or repulse themselves resulting in a deformation of the device [28]. Over the years, numerous varieties of pneumatic soft actuators have been imagined, created, and put to the test, since these devices are low cost, relatively easy to realize, and they are particularly suitable for applications where there is an interaction with man due to their intrinsic compliance. Diverse constructive solutions fall within the broad description of pneumatic soft actuators, and they can be divided into the following four major categories: Pneumatic artificial muscles (PAMs, also known as McKibben muscles), fluidic elastic actuators (FEAs), also known as soft elastic actuators (SEAs), such as Pneu-Nets actuators or soft bending actuators (SBAs), fabric-based actuators, and finally 3D printed actuators are examples of artificial muscles. There are various constructive solutions in each class, some of which define subclasses [19].

This article is focused on the design, production and characterization of a pneumatic soft actuator; more specifically, a silicon PneuNets design based actuator [29] will be investigated.

PneuNets are a type of bio-inspired [30] pneumatic soft actuators that embed in their structure a variable number of chambers connected by a channel. Movement is achieved by pressurizing the internal walls of the actuator: deformation will occur in the least stiff regions causing a bending effect in the structure [31].

Polygerinos et al. proposed in [32] a PneuNets actuator made in silicone (Elastosil) using a two parts mold. The final products are then glued together and a strain limiting layer is added at the bottom part of the actuator. To test the FEM analysis data against experimental results, the position of a single point on the tip of the structure is recorded using a high resolution camera and a third party software to track its trajectory at defined pressure increments. Stano et al. described in [33] the production of a monolithic TPU PneuNets actuator with an embedded strain limiting zone exploiting 3D printing. As stated by the authors the price per part using this technique is around 5€. Characterization is carried out by taking a picture of the inflated actuator placed on a millimeter squared sheet at few pressure samples: the bending angle of the structure is then recorded. FEM analisys has not been performed due to the model complexity. Jiang et al. presented in [34] a fiber reinforced silicone soft actuator obtained from molds, realizing the inner cavity thanks to a prismatic lost wax core. FEM analysis results are verified only through fatigue endurance tests. Bhat et al. in [35] proposed a revisited PneuNets silicon (Dragon Skin 10) based, consisting of an embedded strain limiting 3D printed TPU structure and PLA plates to condition the deformation. The inner cavity is obtained through the use of a hydrosoluble 3D printed PVA core. Characterization is carried out by plotting the position (captured by a high resolution camera) of markers drawn on the actuator on a plane (data is gathered using a third party software). FEM analysis has been conducted but results are not compared to experimental ones.

In this paper simple, cheap and reliable methodologies to produce, characterize and

validate a PneuNets based soft actuator are proposed. The aim is to build a structure similar to the one presented in [32], but exploiting the monolithic design proposed in [33], in order to cut production times and minimize ruptures during inflation. For the sake of simplicity, the strain limiting layer adopted in numerous researches is substituted by a thicker actuator bottom end, to reduce even more the manufacturing steps. A lost wax core is exploited as in [34] in order to obtain a more complex inner cavity geometry compared to the simple prismatic one proposed by Jiang et al.

FEM analysis is conducted on the actuator and experimental deformation data are compared with the theoretical results in order to validate the model. The bending curvature radius is chosen as main characterization parameter; as a matter of fact it can be computed without a fixed reference. A simple and fast characterization routine based on image processing without the need of expensive high resolution cameras is described.

The paper is structured as follows. In Section 2 the main material choice is described and justified, a geometry design is proposed, FEM analysis and data post processing processes are featured, molds production and the actuator manufacturing technique is presented as well as a mechanical characterization setup, and procedural, hardware and software characterization aspects are discussed. Results of the characterization are reported in Section 3. Section 4 contains some key aspects emerged during the various steps of the work. In Section 5 the obtained results are lastly summarized, and future activities are briefly described.

2. Materials and Methods

2.1. Actuator Material Choice

To fabricate a Pneu-Nets soft actuator a good strain tolerant material is needed [36]. The actuator is also expected to regain its initial shape once the deformation is over and to exhibit tolerance to long repetitive cycles. For these reasons, elastomers are often adopted as preferred material for pneumatic soft actuators and more in general for pneumatic soft robotic applications [19]. Marechal et al. in [37] evaluated the mechanical qualities of several different kinds of elastomer, highlighting their stress-strain curves. At first glance, the best possible choice is represented by materials that can reach high values of strain with low stresses, but it has to be taken into account that these properties define a very soft elastomer. At a fixed deformation state, this kind of material will require less input pressure to stay in shape compared to a stiffer one, however it would also exert less force [36]. On the other hand, a highly stiff material will require high values of pressure, making the overall project design more complex in terms of hardware and safety precautions. A silicon rubber with Shore 30A such as Dragon Skin 30 (Table 1 by Smooth-On, Inc., Macungie, PA, USA) seems to represents a good trade off between these two cases [37].

Table 1. Silicon rubber Dragon Skin 30 technical data.

Mixed Viscosity [cps]	Specific Gravity [g/cc]	Specific Volume [cu.in./lb.]	Pot Life [min]	Cure Time [h]	Shore A Hardness [A]	Tensile Strength [psi]	100% Modulus [psi]	Elongation at Break %	Die B Tear Strength [pli]	Shrinkage [in./in.]	Service Temperature Range [°C]
20,000	1.08	25.7	45	16	30	500	86	364	108	<0.001	$-53 \div +232$

2.2. Actuator Geometry

The geometry of the developed soft actuator is based on the PneuNets design, firstly presented by Polygerinos [32], but with a monolithic structure as proposed by Stano in [33]. A mold based fabrication is adopted, with a lost wax core, eliminated through heating.

A section of the overall structure with parametric geometric dimensions is provided in Figure 1.

At the beginning of the design process values of the geometric dimensions have been adopted according to Table 2. Subsequently, FEM analysis (described in detail in Section 2.3) was performed to optimize the value of the thickness of the actuator bottom end (dimension f), by parameterizing the simulation and increasing f at each performed test by 1 mm. The actuator base deformation under pressurization was the quantity considered to identify an optimal value of f. Some constrains were then applied to the results: the maximum bottom face elongation is considered acceptable if it is less then 10% of its initial length, while the total maximum actuator's height has been limited to 20 mm to avoid excessive bulkiness.
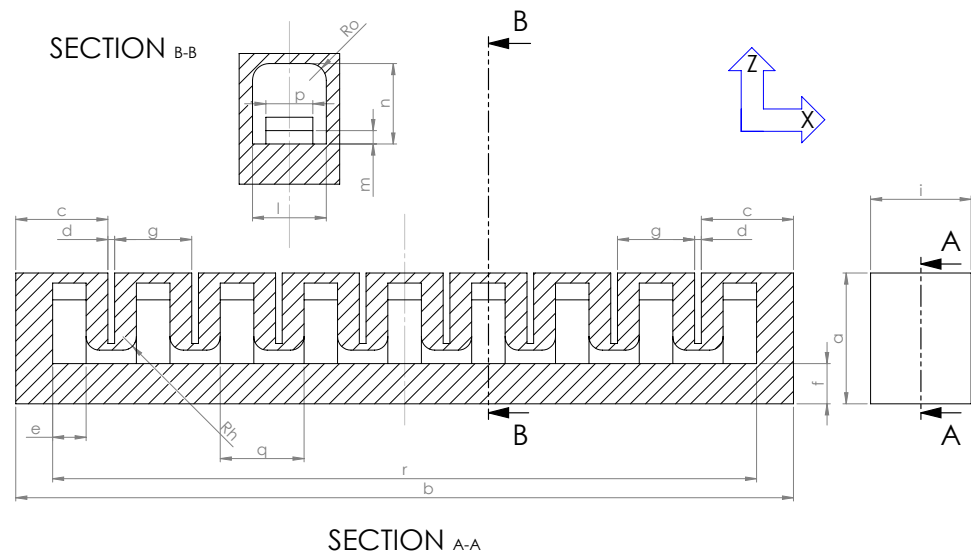

Figure 1. Actuator geometry: starting numerical values of the geometric dimensions are listed in Table 2.

Table 2. Geometric dimensions: symbols and initial values.

Parameter	Value [mm]	Description
a	19.50	Actuator height
b	116	Actuator length
c	13.75	First and last chamber profile length
d	1	Space between chambers
e	5	Chamber cavity length
f	2	Bottom end thickness
g	11.5	Chamber profile length
h	2	Connection radius between chamber and bottom cavity profiles
i	15	Actuator thickness
l	11	Chamber length
m	2	Bottom cavity height
n	12	Chamber height
o	2.5	Top chamber edge-to-edge connection radius
p	7	Bottom cavity thickness
q	12.5	Consecutive chambers step length
r	105	Bottom cavity length

Instead of introducing a strain limiting layer [32], thicker walls have been selected for the regions in which the inner walls deformation should be minimized, as the bottom part and the left and right ends of the structure; thinner regions have been adopted for the opposite purpose. However, it has to be taken into account that thinner walls can cause possible ruptures during inflation and excessively wide chambers will increase the air volume needed to bend the actuator, making the bending movement slower. At the initial stage of the project, manufacturing techniques still needed to be tested: for this reason the here presented geometry does not represent the best possible design, but a starting point that favoured feasibility but which can be largely optimized.

2.3. FEM Analysis and Data Post-Processing

FEM analysis has been conducted in ANSYS environment, on a 3D model of the actuator created with solid modeling CAD. This method proved to be a valid approach for testing the soft actuator motion, forces and stresses, before its actual physical production, i.e., in the design phase. This preliminary analysis allows the optimization of the design choice, as shapes and dimensions.

A valid material model has to be selected: in various researches the Yeoh hyperelastic model is often exploited as it can accurately represent the behaviour of an elastomer under external forces [38]. Two sets of Yeoh parameters for Dragon Skin 30 silicon rubber have been gathered from literature: for our application, the one proposed by Marechal et al. [37] proved to describe a too stiffer model while the Matheus et al. [39] has shown to represent a too soft actuator. This is probably due to the geometry of PneuNets design and to non-idealities between theoretical and experimental characterization. A new model has been built using a mean between the two sets of parameters (Table 3).

Table 3. Yeoh hyperelastic model parameters.

Reference	C_1 [MPa]	C_2 [MPa]	C_3 [MPa]
Marechal et al. [37]	1×10^{-1}	1.19×10^{-1}	6.04×10^{-4}
Matheus et al. [39]	1.1488×10^{-1}	1.262×10^{-3}	0
Proposed model	1.0744×10^{-1}	6.01×10^{-2}	3.02×10^{-4}

At this point, a coordinate system has been defined at each external chamber sector of the geometry, for a total of eight (Figure 2a). Noted that the deformation will occur along a circular profile, the idea was to gather the position of eight points on the surface of the actuator (initially resting at the center of their defined coordinate system) and to extract the radius of the circle, calculated through interpolation, in order to describe the deformation state at each input pressure with just one parameter.

The input pressure has been defined as a ramp between 0.1 bar and 1.15 bar acting on the internal walls of the structure (Figure 2b): since the maximum tolerable pressure of the actuator is not initially known, the final ramp value was increased at each FEM simulation run until the overall structure's safety factor was in the range of 2 to 3. The pressure ramp acts over a simulation time span of 1 s.

The safety factor (*SF*) is defined as:

$$SF = \frac{Ultimate\ Tensile\ Strength}{1st\ principal\ stress} \tag{1}$$

By providing to ANSYS engineering data Dragon Skin 30 tensile strength, declared as 500 psi (Table 1), the safety factor can be automatically computed by the software. Its minimum value was chosen as 2 to compensate for any discrepancies between the simulated and real models. In this way, the actuator should be able to withstand twice the breaking stress claimed by the material manufacturers. From tests conducted, a minimum safety factor value greater than 3 is achievable, without changes to the already optimized

geometry, by significantly reducing the actuator inlet pressure, but this causes heavy drops in force development. The final value was therefore chosen in the described range.

SF is obtained by applying a stress probe in ANSYS once the simulation setup is complete (Figure 2h).

Additional geometry (Figure 2c) has been inserted in order to simulate the physical interaction between the soft actuator and the mechanical characterization setup (in-detail described in Section 2.5). Two small plates made of structural steel will lock the first chamber in its resting position during the characterization process and represent fixed faces in the simulation.

The action of gravity is defined along the Z axis described in Figure 1: this is consistent with the configuration that will be adopted during the experimental characterization process.

Finally, meshing has been carried out optimizing aspect ratio, jacobian ratio and skewness parameters of the finite elements (Figure 2d). In order to perform geometry optimizations as above described, meshing has been carried out with the aim of obtaining a fast simulation: in this way a good number of simulations could be performed within a reasonable time. The use of linear and quadratic elements is investigated in Section 3.1. All the FEM operations in this article are executed using the adopted mesh. A comparative analysis is carried out over different number of elements. The numerical description of the adopted model is presented in Table 4.

Once a static structural type simulation is complete, deformation data for each point are presented by Ansys in a chart as 3 linearly interpolated curves, reporting the related movements, with respect to time, along X, Y and Z direction relative to the resting positions (Figure 2i). Data represented by the movements of the single eight points, can be exported in `.txt` format for post processing procedures: this file will contain the position of each point relative to its coordinate system center at multiple pressure increments. Stress data has also been exported with the same method (Figure 2e).

Force evaluation has been conducted inserting in the model a fixed face in contact (assumed frictionless) with the bottom part of the actuator: the force reaction of the upper face has been then probed and exported (Figure 2f). Results are represented by the reaction's magnitude in Newtons with respect to simulation time.

The overall elapsed time needed to carry out the FEM simulation was 8 min.

To check whether a strain limiting layer is needed a mean strain probe is applied to the bottom face of the actuator (Figure 2g): its mean absolute elongation is then evaluated as $\epsilon = \frac{\delta}{L}$, with ϵ being the mean strain, δ the mean absolute elongation and L the actuator's bottom face length while not pressurized.

Overall, simplifications made are as follows:

- Contact between pressurized chambers is assumed frictionless;
- Contact between the locking mechanism and the involved actuator portion (Figure 2c) is assumed bonded;
- Contact between the fixed face adopted in force evaluation and the involved actuator portion (Figure 2f) is assumed frictionless;
- The mean elongation of the bottom face is assumed to be acting exclusively along the direction of the X axis (Figure 2g);

Data post processing has been carried out by passing the ANSYS measurements to a MATLAB script. To track movements under inflation, this script builds multiple structures containing the position of the eight points relative to their coordinate system at a defined pressure step. Then, a circle is fitted through the points position using the Pratt numerical method [40] which is fast in terms of computation and can provide good approximations for our application. The calculated radii at each stage are then fitted in order to obtain a theoretical radius-pressure mathematical model.
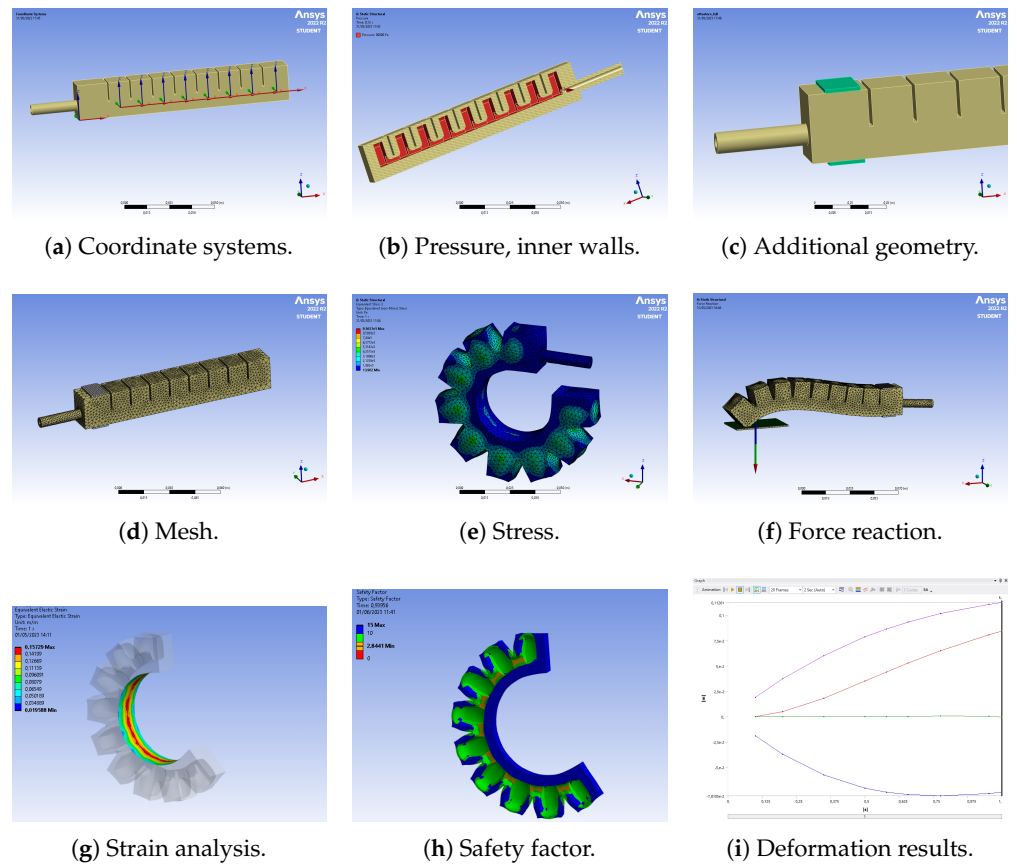
(**a**) Coordinate systems.

(**b**) Pressure, inner walls.

(**c**) Additional geometry.

(**d**) Mesh.

(**e**) Stress.

(**f**) Force reaction.

(**g**) Strain analysis.

(**h**) Safety factor.

(**i**) Deformation results.

Figure 2. ANSYS static structural stages.

Table 4. Mesh parameters, AVG = average, SD = standard deviation.

Parameter	Value
Aspect ratio	AVG: 1.88 *SD* : 0.46
Jacobian ratio	AVG: 1 *SD* : 0
Skewness	AVG: 8.78×10^{-5} *SD* : 0.13
Element quality	AVG: 0.83 *SD* : 9.64×10^{-2}
Element type	LINEAR
Capture curvature	YES
Capture proximity	YES
Nodes	21,962
Elements	99,592

2.4. Mold and Core

In order to adopt a cheap solution for the manufacture of presented soft actuators, the technique of casting silicone with a wax core is considered. For this purpose, the elastomer needs to be poured into an appropriate mold. A first version of the mold has been realized in ABS by 3D printing in two parts, as shown in Figure 3a: with this choice extraction problems arise, as the elastomer sticked to the mold walls due to their rough texture, causing ruptures (Figure 3b). To avoid this, a new version of the mold in three parts (upper, middle, bottom) has been built in three parts (Figure 3c). With this constructive choice, it is possible to exert an even force on the bottom part of the cast to slowly extract it (Figure 3d).
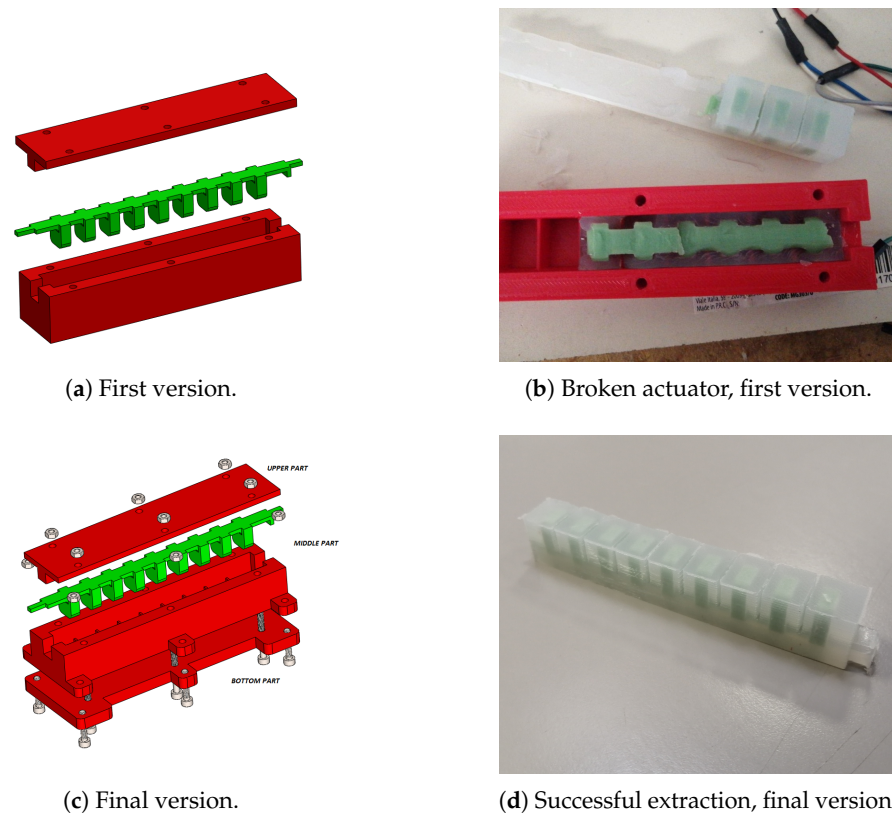
(**a**) First version.

(**b**) Broken actuator, first version.

(**c**) Final version.

(**d**) Successful extraction, final version.

Figure 3. Mold versions.

Hollow cavities of the structure are obtained through the use of a lost core. At first, an hydro-soluble material such as PVA [41] had been considered, as it can be 3D printed with high precision. However, the time required for the PVA to melt is long. To speed up the process, of dissolution but also of production of the core, wax was preferred. Thanks to wax low melting point, the core can be easily produced with an overall good precision with a casting melted wax process. A silicone mold (done with Dragon Skin 30 silicone), as shown in Figure 4b, has been realized from a PLA hard one (Figure 4a). Figure 4c shows the wax core in the silicone mold. The mold flexibility makes the extraction process fast and reliable.

(**a**) ABS mold.

(**b**) Dragon Skin 30 mold.

(**c**) Poured wax.
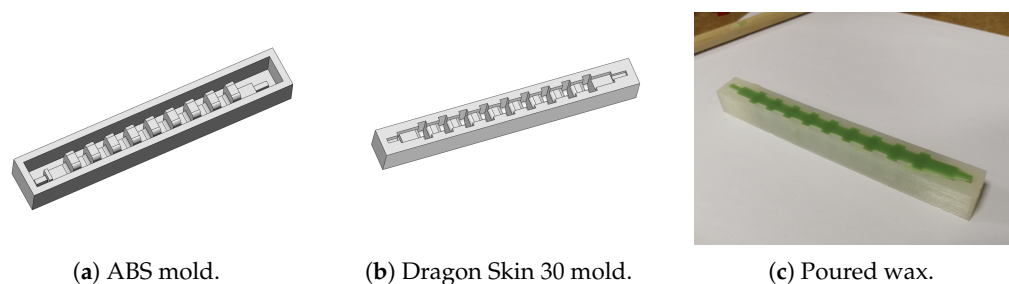
Figure 4. Wax core production.

The actuator production consists of the following steps:

- production of the wax core by casting in the silicone mold;
- 60 mL of elastomer are produced (30 mL part A + 30 mL part B of Dragon Skin 30 silicone) and hold in vacuum for at least 10 min to extract air;
- silicone casting in the ABS + wax core mold;
- silicone cure for at least 24 h;

- the actuator is heated in an oven at 70 °C until the whole wax core melted. Silicone properties should be preserved since the melting temperature is within the operating range described in Table 1.

A tube could now be inserted into one of the leftover hollow cavities, held in place by a flange (Figure 5b,e) made of Dragon Skin 30 and glued to the actuator with silicon glue (Sil-Poxy by Smooth-On Inc.). In order to minimize air leaks, a kevlar wire can be wrapped around the cylindrical part of the flange. The other end of the actuator is simply sealed with silicon glue (still Sil-Poxy glue). The finished product is shown in Figure 5c.

It is worth noticing that if the top part of the mould is not properly sealed and the air extraction process from the silicone is not efficient, bubbles can generate damaging the structure (Figure 5d): if so, a filler of Dragon Skin 30 is needed.
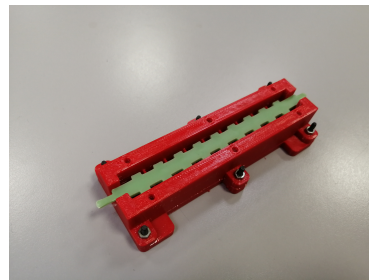
(**a**) Mold and wax core.
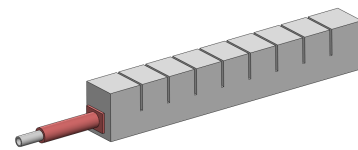
(**b**) Flange (red part).

(**c**) Final product.

(**d**) Damaged actuator.

(**e**) Flange mold.

Figure 5. Actuator production.

2.5. Experimental Characterization Setup

A mechanical structure (Figure 6) has been realized in order to support the actuator during the characterization procedure. It is composed of three parts: base, slider and clamp. The slider mechanism is used to adjust the height of the actuator from the base, while the clamp holds the system in place during pressurization.
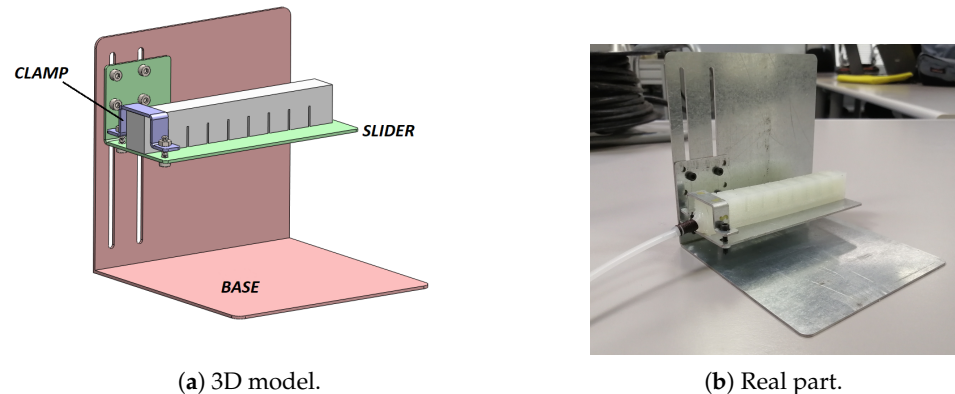
(**a**) 3D model.

(**b**) Real part.

Figure 6. Mechanical structure for the actuator fixing for the characterization process.

An open loop pressure control is adopted for the actuator characterization. Two different modes to control pressure have been provided and compared:

- Electronic pressure control. Pressure is provided by an electronic pressure regulator (Regtronic, Metal Work SpA) controlled by an Arduino Uno microcontroller through 0–5 V PWM output (Figure 7a).
- PWM pressure control. Another purpose of this research is to evaluate actuation through direct PWM pressure control: to do this, an electrovalve (V114-5G, SMC) is controlled by an Arduino Mega at a frequency of 20 Hz. Schematics are provided in Figure 7b,c.

In both cases, a GoPro Hero 7 Silver camera is mounted in front of the mechanical setup to catch the soft actuator deformation state at each input pressure value. The camera choice was driven by its low price and the possibility to provide a local WiFi network through which commands can be sent from an external device.

A blank white sheet is put behind the mechanical structure to minimize background disturbances and light reflections: this is important in order to minimize object detection problems during image processing, as further described in Section 2.6.2.
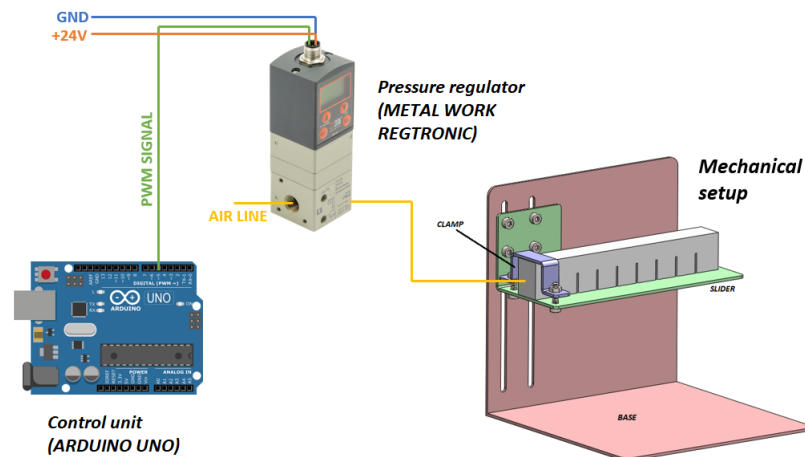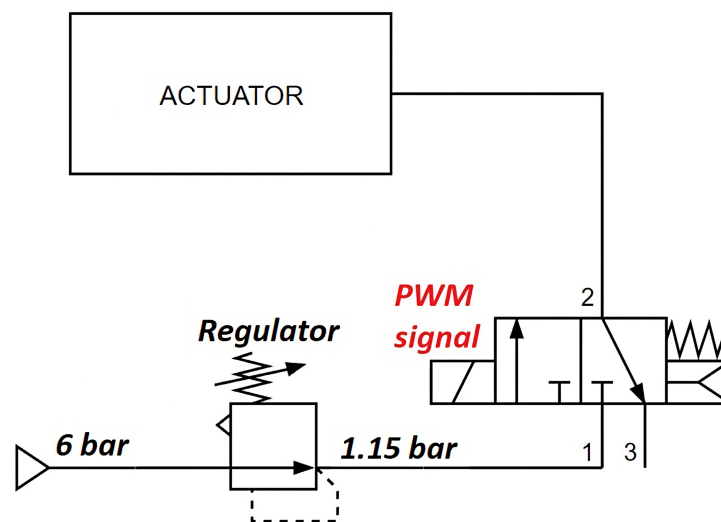

(**a**) Electronic pressure control.

Figure 7. *Cont.*
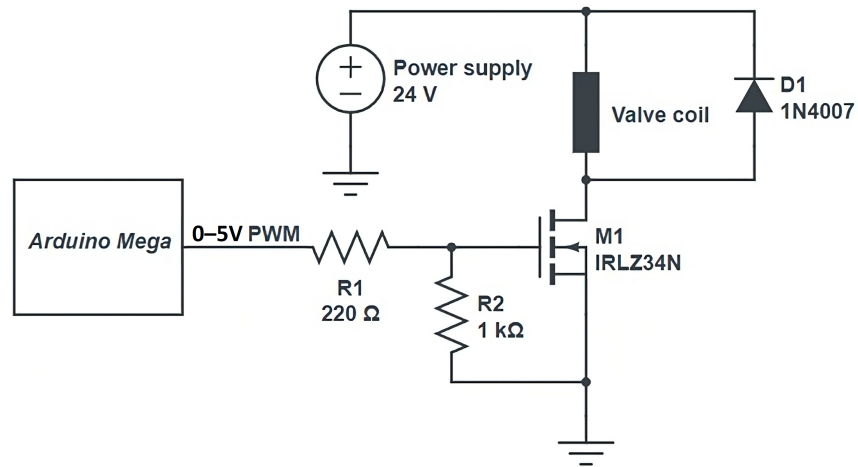
(**b**) PWM pressure control, electrical schematic.

(**c**) PWM pressure control, pneumatic diagram.

Figure 7. Developed and compared pressure control modes for actuators characterization.

2.6. Experimental Characterization Procedure

2.6.1. Data Acquisition

A Python script has been realized in order to send the desired pressure value to an Arduino Uno via serial port. Once the message is deployed, Arduino will communicate with the Regtronic pressure regulator through a PWM signal. The script will then wait for a customizable stabilization time: the actuator will in fact oscillate for a brief period due to inertial effects every time a new pressure value is set. When the waiting time expires, the script will send to GoPro a video start signal followed by its duration: once the video is ended, the routine will start again. Communications between script and camera are made possible thanks to the goprocam Python library. At the end of the procedure, videos can be downloaded to a PC for image processing. The chosen camera requires additional care in image processing due to its fisheye len. A workflow summary is presented in Figure 8.
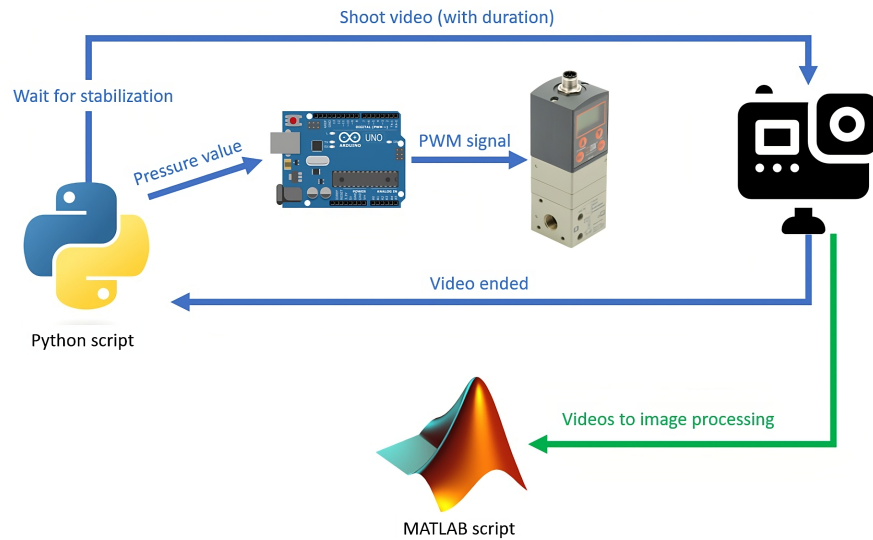
Figure 8. Data acquisition flow.

2.6.2. Image Processing

All the image processing procedures are executed in the MATLAB environment. The procedure is graphically summarized by the diagram in Figure 9.
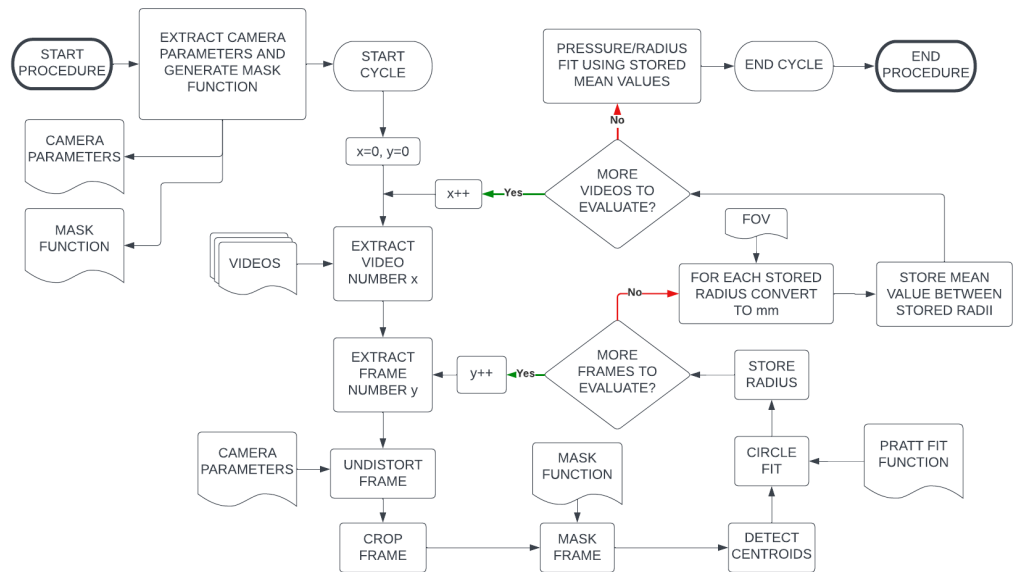

Figure 9. Image processing workflow.

Red markers are drawn on the actuator at the same locations in which the coordinate systems were defined in FEM analysis (Figures 2a and 10a). During videos acquisition the camera must stay as parallel as possible to the scene and always at the same distance. To get the current field of view, a picture to a metric reference should be taken at the beginning of the operation with the same camera in the same position (Figure 10b). A camera calibration procedure is therefore required.

The single tasks of the image processing sequence are described in detail below.

1. *Camera calibration* Fisheye lens distortion needs to be corrected (Figure 10e). A sample of 20 checkerboard images shot from different angles and distances are sent to MATLAB's Camera Calibrator App exploiting the fisheye distortion option (Figure 10c). The app provides camera intrinsic and extrinsic parameters as output by defining the real squares dimensions composing the checkerboard.

2. *Color mask generation*. We are only interested in the red markers position: therefore, every other element contained in the videos can represent disturbances. A single frame of a video is loaded into MATLAB's Color Thresholder App. By excluding other colors but red, only the markers should be visible on the preview image (Figure 10d). Once this is achieved, the obtained mask can be exported as a MATLAB function.

3. *Frame extraction*. Every video shot is referred to a different pressure value applied to the actuator. For each video, every frame composing it is extracted to be processed as a single image.

4. *Image undistortion*. Each single frame is undistorted (Figure 10f) using the `undistort-FishEyeImage` function (previously generated intrinsic parameters are passed as inputs).

5. *Image cropping*. Image undistortion can cause the presence of black areas at the border of the frame due to the "shrinking" effect generated by fisheye correction. The frame should be cropped in order to exclude those areas.

6. *FOV evaluation (to be performed once before the characterization program starts)*. An undistorted, cropped image of a metric reference is used to evaluate the resulting image field of view (Figure 10b).

7. *Image masking*. The red mask is applied to each frame by calling the generated function: a black and white image is returned (Figure 10g). If markers appear to be inhomogeneous, the `imfill` function can be used with the 'holes' parameter to "fill" the white objects.

8. *Centroids detection*. At this point, red markers should be represented as white, distinct objects over a black background. The MATLAB function `regionprops` with the 'Centroid' parameter provides as output the x and y coordinates of these object centroids in pixels (Figure 10h).

9. *Circle fit*. X and y centroid coordinates are then passed as input to the Pratt circle fit method function (the same used in FEM analysis data posto-processing) and the radius value is extracted and stored (Figure 10i). The final radius is set as the mean value between the radii extracted from each frame of a single video.

10. *Iteration*. Steps 3 to 9 (except 6) are repeated for each video acquired in the characterization run.

11. *Pixel to millimeter conversion*. With the last video processed, the radius values are converted to millimeters using the formula $radius[mm] = radius[px] \times \frac{FOV[mm]}{frame\ lenght[px]}$.

12. *Pressure-radius fit*. Finally, pressure-radius values are fitted in order to obtain a proper mathematical relation.

2.6.3. Experimental Force Evaluation

Force evaluation has been carried out by placing the actuator on a kitchen scale with 1g resolution while locked on the mechanical setup (off the scale). The slider was put on the same level of the scale in order to avoid tensions in the actuator due to misalignment between the two planes (Figure 11): to do this, a good method is to first weight the "free" soft actuator and then to slowly move the slider until the weight is about the same. Data has been collected at given pressure values, converted in Newtons and then compared to the theoretical FEM forces.
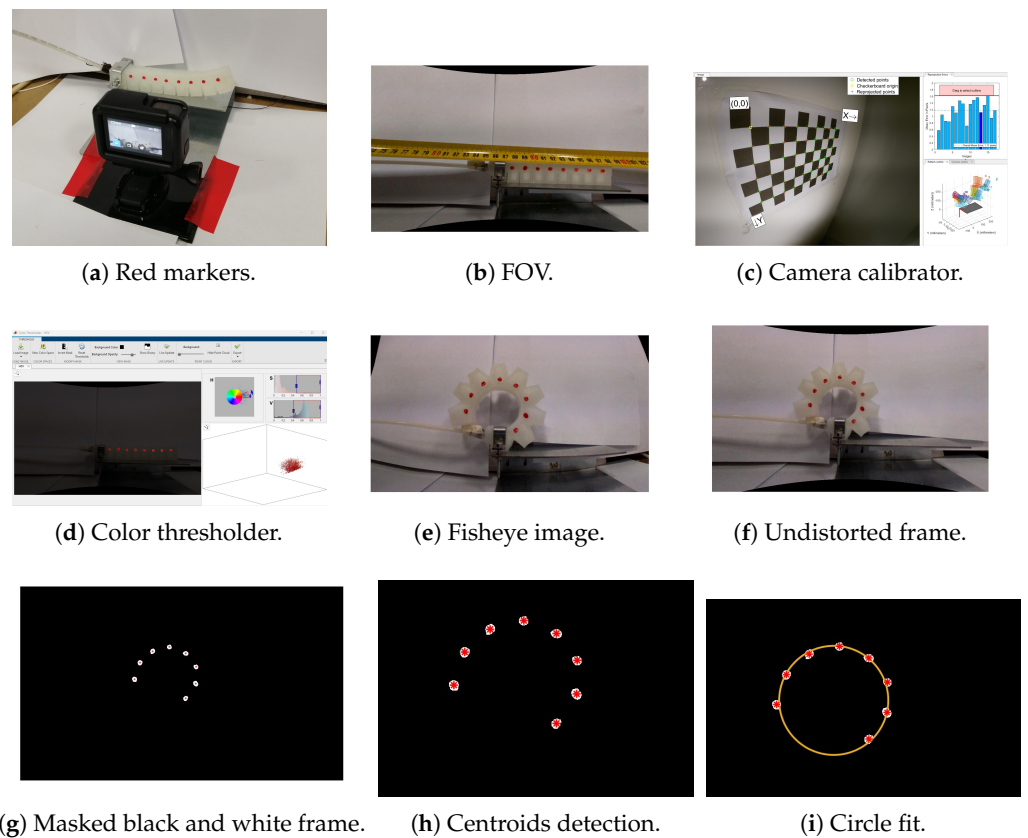
(**a**) Red markers.

(**b**) FOV.

(**c**) Camera calibrator.

(**d**) Color thresholder.

(**e**) Fisheye image.

(**f**) Undistorted frame.

(**g**) Masked black and white frame.

(**h**) Centroids detection.

(**i**) Circle fit.

Figure 10. Image processing procedural steps.

Figure 11. Force evaluation procedure.

3. Results

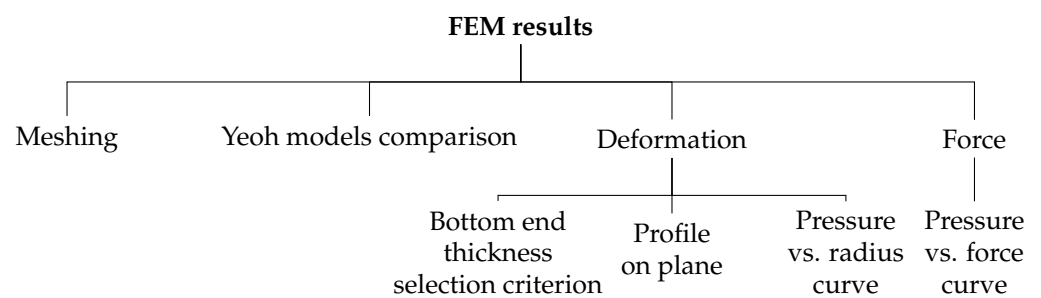In this section the results of characterization based on FEM analysis and on experiments are reported, for the correlations and quantities listed in Figure 12 and 13.

Figure 12. FEM results diagram.
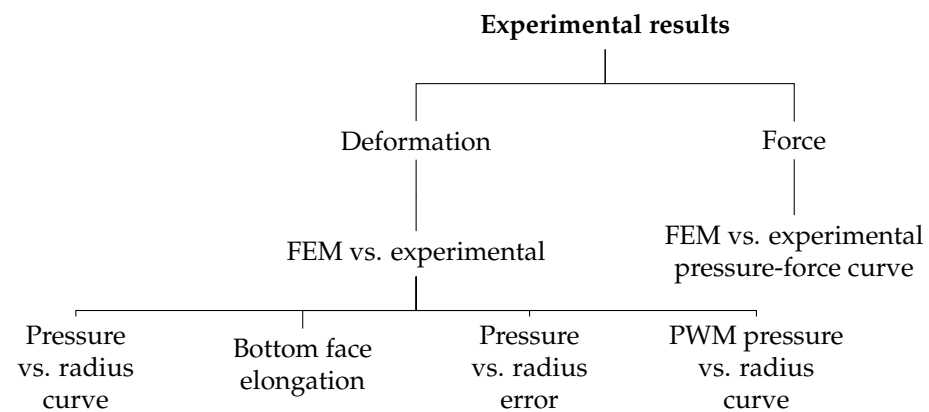
Figure 13. Experimental results diagram.

3.1. Meshing

As described in Section 2.3, a suitable mesh model for a "fast" simulation was needed. The mesh model presented in Table 4 resulted from a comparative test conducted with linear and quadratic elements adopted in the same model. Numerical values for tested cases are reported in Tables 5 and 6. Simulations with mesh based on linear elements proved to be much faster compared to the one with quadratic elements. Moreover, in the former the minimum safety factor falls in the range 2–3, while in the latter is greater than 3. For speed of simulation and safety reasons, this was the chosen model.

Table 5. Mesh parameters, linear elements.

Parameter	Value
Element type	LINEAR
Nodes	21,962
Elements	99,592
Safety Factor	2.4
Simulation time	448 s

Table 6. Mesh parameters, quadratic elements.

Parameter	Value
Element type	QUADRATIC
Nodes	153,618
Elements	99,463
Safety Factor	3.1
Simulation time	2499 s

Deformation-wise, pressure vs. radius curves, gathered as described in Section 2.3, show a trend of convergence to the same final value as represented in Figure 14.

The same test was then repeated for meshes with different element count as reported in Table 7 with M1 being the model built automatically by the software and M4 the initial model proposed in Section 2.3. As presented in Figure 15 the curves are practically overlapping. However, the safety factor value is shown to decrease as elements count increase. Since it was over 1 in the M1 case and simulation time was over 28 min, it was decided to test the actuator's resistance to pressurization experimentally. As reported in Section 3.4, the structure was able to handle pressure values up to 1.15 bar without any issue during the whole characterization procedure.
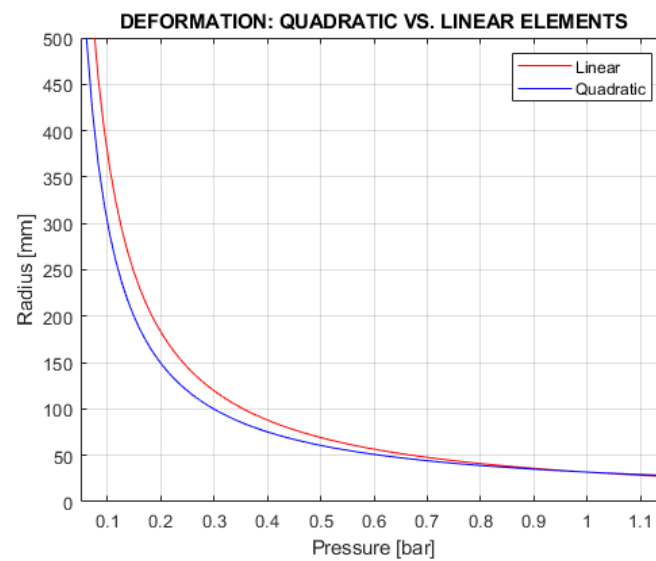
Figure 14. Deformation data, linear vs. quadratic elements.

Table 7. Mesh models tested, linear elements.

Model Name	Nodes	Elements	Safety Factor	Simulation Time
M1 (automatic)	95,853	427744	1.3	1709 s
M2	76,249	328,517	1.5	1331 s
M3	45,355	213,369	1.8	687 s
M4	21,962	99,592	2.4	448 s
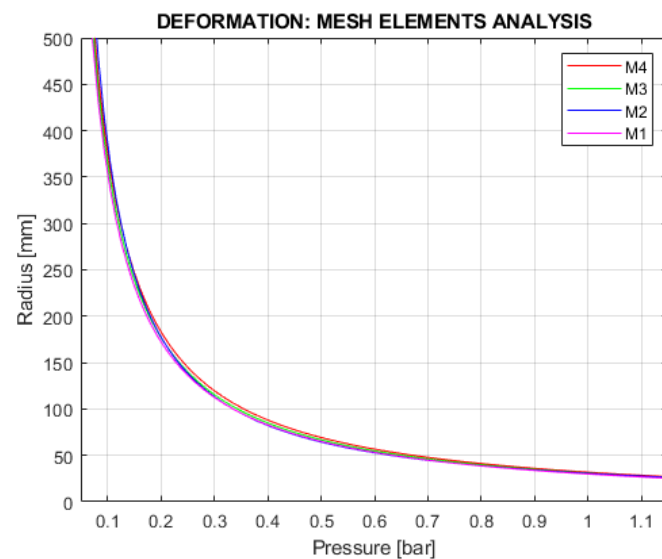
Figure 15. Deformation data, tested mesh models.

3.2. Bottom End Thickness Selection Criterion

Parameterized FEM analysis tests have been conducted as described in Section 2.2. Resulting total bottom face elongation modulus and total actuator height are plotted against different bottom thickness values (Figure 16). The first elongation modulus point to fall among the acceptable elongation values is the one identified at the bottom thickness value of 6mm. This particular value was then selected as the actuator final bottom end thickness.
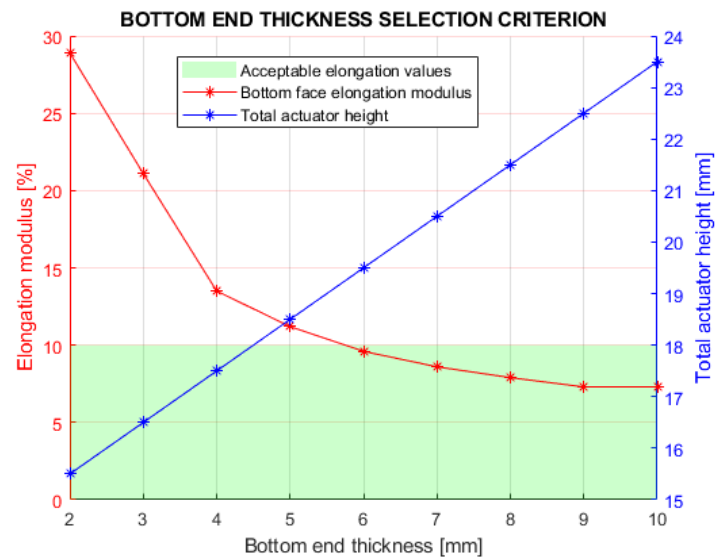
Figure 16. Bottom end thickness selection criterion results.

3.3. Actuator Characterization Based on FEM Analysis

Yeoh model have been evaluated by obtaining the actuator radius at different pressures, as described in Section 2.3. The characterization points and the curve of the radius as a function of the pressure are plotted in Figure 17. The results based on the presented model (Section 2.3) are compared with the ones presented in literature by Marechal et al. [37] and Matheus et al. [39].
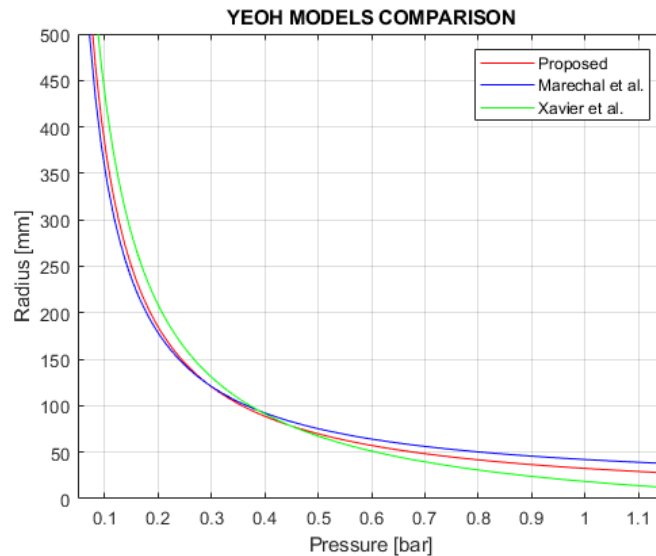
Figure 17. Yeoh models comparison.

The actuator's deformation state at different pressures is represented by the position of the considered eight points using the developed Yeoh model, as shown in Figure 18.

In Figure 19 the punctual values of the calculated radius at different pressures are reported, with the interpolating curve superimposed.

The developed force at the actuator extremity for different input pressures estimated through the FEM analysis (Figure 2f) is reported in Figure 20: single points and the fitting curves are practically overlapping.
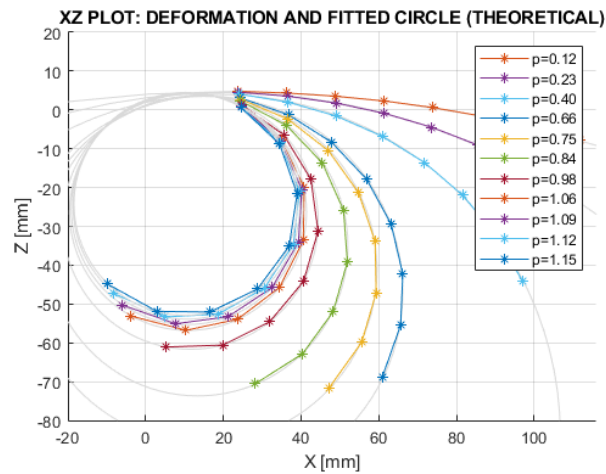
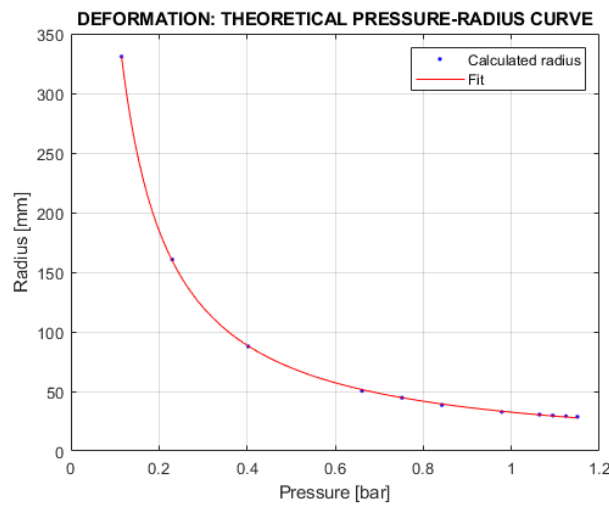**Figure 18.** Deformation and fitted circle (p = pressure value).

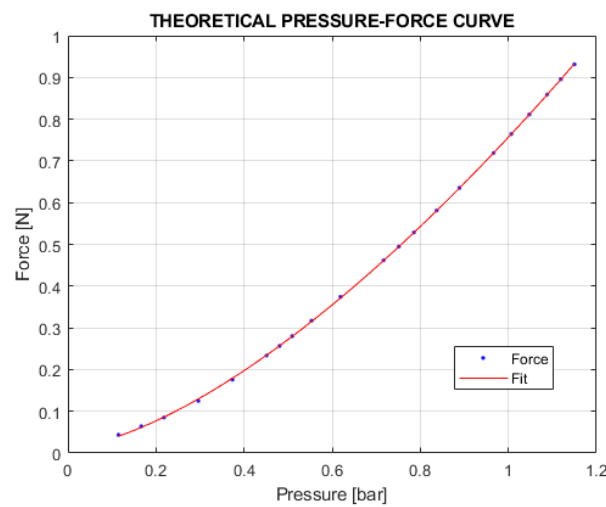**Figure 19.** Theoretical pressure-radius curve.

Figure 20. Theoretical pressure-force curve.

3.4. Actuator Experimental Characterization

For the experimental determination of the radius vs pressure correlation the routine of Figure 9 has been executed for two actuator samples and experimental deformation data

are compared to the simulated ones (Figure 21). A deviation curve between simulated and experimental data is plotted in Figure 22. The results of the experimental force estimation, compared with the ones obtained in simulations for the Sample 1, are shown in Figure 23. PWM pressure input is tested and deformation data are plotted in Figure 24.
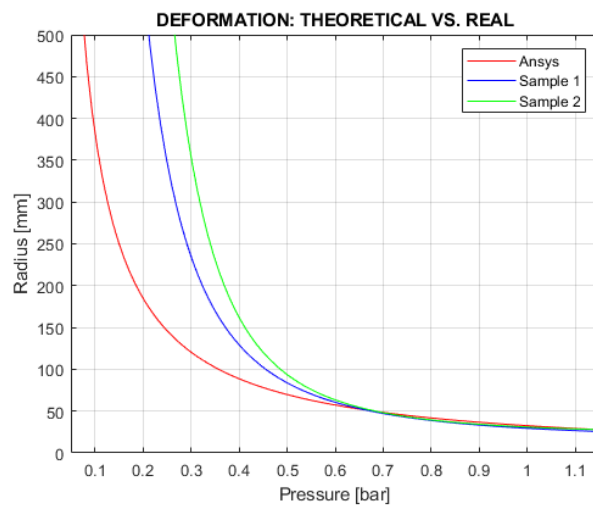

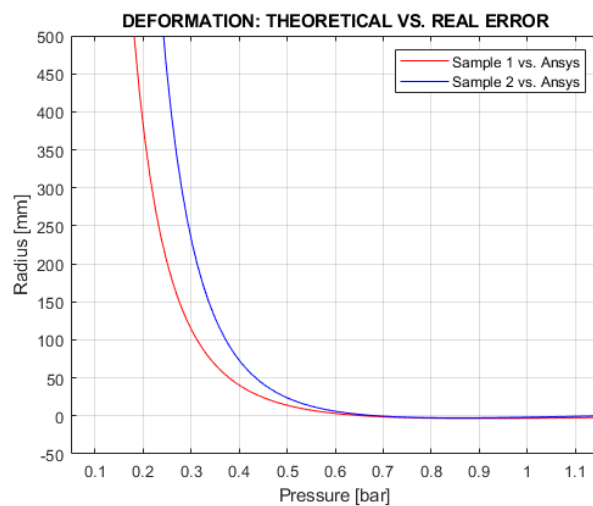**Figure 21.** Deformation: theoretical vs. real (2 samples).

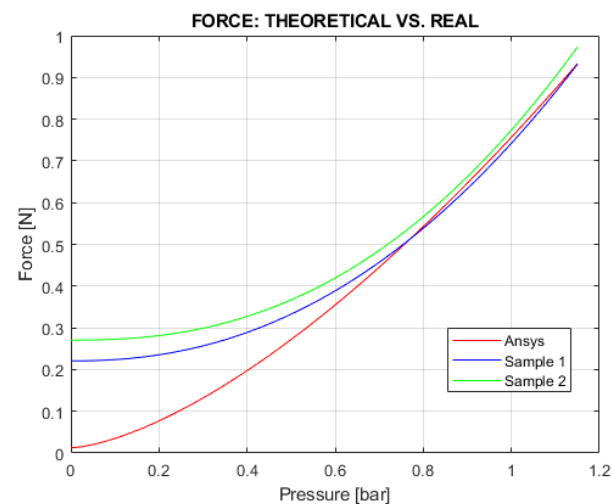**Figure 22.** Deformation: simulated and experimental curves deviation.

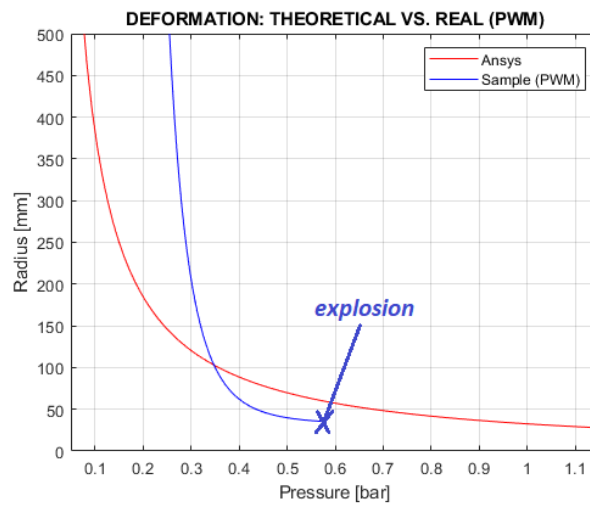**Figure 23.** Force: simulated vs. experimental.

Figure 24. Deformation: simulated vs. experimental (PWM).

All fitting operations are executed with MATLAB's `fit` command using the `power2` model. Therefore, the mathematical expression between output (y) and input (x) data is:

$$y(x) = a \times x^b + c \tag{2}$$

with a, b, c being appropriate constants.

The fitting curves parameters values for the radius vs pressure and force vs pressure simulated and experimental curves are resumed in Table 8.

Table 8. Fitting curve parameters.

Experiment	a	b	c
Deformation: FEM (Ansys) data	35.29	−1.04	−2.72
Deformation: sample 1	14.08	−2.28	15.37
Deformation: sample 2	8.94	−3.00	21.97
Force: FEM (Ansys) data	0.74	1.52	0.012
Force: sample 1	0.52	2.22	0.22
Force: sample 2	0.50	2.38	0.27

3.5. Actuator Experimental Bottom Face Elongation

From FEM results, the theoretical mean absolute elongation at the bottom face of the actuator is 9.6% of its initial length. Two undistorted frames (deflated and final experimental pressure value) are loaded into Solidworks to check the starting and final length of the bottom face. In that case the elongation value is about 9.1% (11 mm), validating the theoretical value and describing a shrinking effect due to high deformation in the top part of the actuator. The value was considerate as acceptable since the ends of structure will be locked on a subject's finger in some way. Measurements shown in Figure 25 don't represent the actual scale since only a ratio between the two cases was needed.
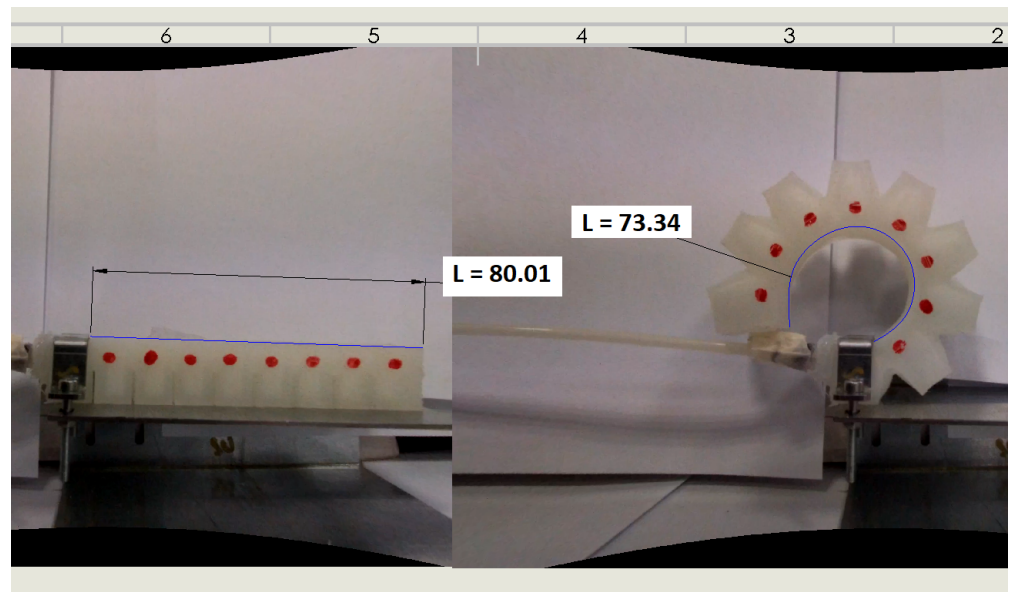
Figure 25. Experimental length estimation for comparison with simulations.

4. Discussion

From obtained results, the following conclusions arise.

A wax core and a 3D printed mold can be used in the actuator production with good results. No damage is reported after heating the structure in order to melt the core.

A strain limiting layer is not strictly needed with the proposed geometry.

The cost per part is about 1.8 €/pc. Molds costs are not included since their production is to be performed once.

By choosing an appropriate material model, FEM analysis can be conducted with good results in order to predict a PneuNets soft actuator's real behaviour under pressurization: error curve shows a deviation from theoretical radii data of just above 3 mm in the pressure range 0.6–1.15 bar (the maximum adopted pressure). Force-wise deviation is about 0.02 N in the same pressure range.

For "low" input pressure, deformation and force values significantly deviates from theoretical ones, probably due to non-idealities in the characterization setup: as a matter of fact external forces, such as friction between the actuator and the mechanical structure elements, can distort experimental results. Furthermore, for low pressure values the Pratt method tries to interpolates a huge circle with few points very close to each others. Another non-ideality can be represented by mechanical tensions generated by the connected tube stiffness.

A GoPro camera can provide enough image quality to perform a characterization procedure upon proper calibration.

Experiments developed with PWM pressure control with SMC V114-5G valves reveal that this does not represent a good pressure supply control approach: not only the actuator exploded at about 50% of the test work cycle, but also deformation data shows high deviations from the theoretical ones. Since the valves maximum operating frequency was only 20 Hz, tests should be repeated with better performing valves.

A final test has been conducted by gluing a Velcro stripe on the actuator bottom end using Sil-Poxy silicon glue. The whole system has then been fixed on a healthy subject's hand and a 1.15 bar pressure value has been provided. The soft actuator exerted enough force to bend the index finger (Figure 26b).

Data have not been gathered from this test since the focus of this research was on the actuator production and characterization. Future researches will relate more on the actuator application for robotic rehabilitation matters.
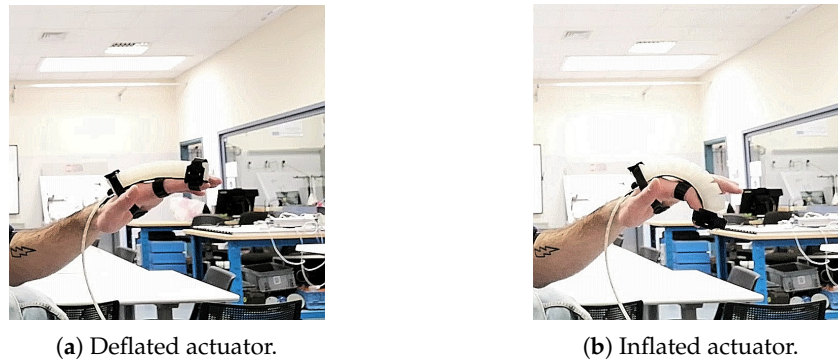
(**a**) Deflated actuator.　　　　　　(**b**) Inflated actuator.

Figure 26. Final test.

As an example of applying the actuator to an exoskeleton for hand rehabilitation, a very preliminary version with only one actuated finger is shown in Figure 27: the actuator is connected to a wrist support and fingers through Velcro stripes.

(**a**) Top view.　　　　　　(**b**) Lateral view.

Figure 27. Assembled glove.

5. Conclusions

The paper presents methodologies to design, produce and characterize PneuNets soft actuator. In particular, a design method which allows optimization, a rapid and economical manufacturing technique and a simple characterization method, with inexpensive equipment has been proposed.

The cheap and easy production is guaranteed by a monolithic design realized through the use of 3D printed molds and a lost wax core: this allowed to cut production steps and costs compared to other related approaches. FEM analysis has been conducted to gather preliminary data about the structure properties and results have been evaluated and confirmed with experimental tests, featured by image processing techniques. The experimental validation of the FEM based simulation justifies the use of this tool for the optimized design of different geometries.

With production methodologies validated, future work will be related on geometry optimizations for hand rehabilitation purposes.

A further development can be represented by the insertion of a sensor in the production phase in order to have movement feedback directly integrated in the actuator. The integration in the actuator of graphite-based flex sensors [42] or sensory actuating hydrogel [43] or other sensors [44] could allow the development of soft actuators with greater functionality and complexity, also with the potential to develop AI based condition monitoring solutions [45,46].

Author Contributions: Conceptualization, M.T. and D.L.; methodology, M.T. and D.L.; formal analysis, M.T. and D.L.; data curation, M.T. and D.L.; writing—original draft preparation, M.T. and D.L.; writing—review and editing, M.T. and D.L. All authors have read and agreed to the published version of the manuscript.

Funding: This research received no external funding.

Data Availability Statement: Not applicable.

Conflicts of Interest: The authors declare no conflict of interest.

References

1. Hunter, S.; Crome, P. Hand function and stroke. *Rev. Clin. Gerontol.* **2002**, *12*, 68–81. [CrossRef]
2. Agarwal, P.; Deshpande, A.D. Exoskeletons: State-of-the-Art, Design Challenges, and Future Directions. In *Human Performance Optimization: The Science and Ethics of Enhancing Human Capabilities*; Oxford University Press: Oxford, UK, 2019. [CrossRef]
3. Tiboni, M.; Borboni, A.; Vérité, F.; Bregoli, C.; Amici, C. Sensors and Actuation Technologies in Exoskeletons: A Review. *Sensors* **2022**, *22*, 884. [CrossRef] [PubMed]
4. Polygerinos, P.; Wang, Z.; Galloway, K.C.; Wood, R.J.; Walsh, C.J. Soft robotic glove for combined assistance and at-home rehabilitation. *Robot. Auton. Syst.* **2015**, *73*, 135–143. [CrossRef]
5. Rehmat, N.; Zuo, J.; Meng, W.; Liu, Q.; Xie, S.Q.; Liang, H. Upper limb rehabilitation using robotic exoskeleton systems: A systematic review. *Int. J. Intell. Robot. Appl.* **2018**, *2*, 283–295. [CrossRef]
6. Ertas, I.H.; Hocaoglu, E.; Patoglu, V. AssistOn-Finger: An under-actuated finger exoskeleton for robot-assisted tendon therapy. *Robotica* **2014**, *72*, 1363–1382. [CrossRef]
7. Bin Imtiaz, M.S.; Babar Ali, C.; Kausar, Z.; Shah, S.Y.; Shah, S.A.; Ahmad, J.; Imran, M.A.; Abbasi, Q.H. Design of portable exoskeleton forearm for rehabilitation of monoparesis patients using tendon flexion sensing mechanism for health care applications. *Electronics* **2021**, *10*, 1279. [CrossRef]
8. Serpelloni, M.; Tiboni, M.; Lancini, M.; Pasinetti, S.; Vertuan, A.; Gobbo, M.; Meccanica, I.; Brescia, U. Preliminary Study of a Robotic Rehabilitation System Driven by EMG for Hand Mirroring. In Proceedings of the IEEE International Symposium on Medical Measurements and Applications (MeMeA), IEEE, Benevento, Italy, 15–18 May 2016; pp. 16–21.
9. Tiboni, M.; Legnani, G.; Lancini, M.; Serpelloni, M.; Gobbo, M.; Fausti, D. ERRSE : Elbow Robotic Rehabilitation System with an EMG-Based Force Control. In *Mechanisms and Machine Science*; Springer: Berlin/Heidelberg, Germany, 2018; Volume 49.
10. Rticle, C.R.A.; Haghshenas-jaryani, M.; Patterson, R.M.; Pt, N.B.; Wijesundara, M.B.J. A pilot study on the design and validation of a hybrid exoskeleton robotic device for hand rehabilitation. *J. Hand Ther.* **2020**, *33*, 198–208. [CrossRef]
11. Amici, C.; Ghidoni, M.; Ceresoli, F.; Gaffurini, P.; Bissolotti, L.; Mor, M.; Fausti, D.; Antonini, M.; Ragni, F.; Tiboni, M. Preliminary Validation of a Device for the Upper and Lower Limb Robotic Rehabilitation. In Proceedings of the 2019 23rd International Conference on Mechatronics Technology (ICMT), Salerno, Italy, 23–26 October 2019; pp. 1–6. [CrossRef]
12. Hwang, B.; Jeon, D. A method to accurately estimate the muscular torques of human wearing exoskeletons by Torque sensors. *Sensors* **2015**, *15*, 8337–8357. [CrossRef]
13. Amici, C.; Ragni, F.; Ghidoni, M.; Fausti, D.; Bissolotti, L.; Tiboni, M. Multi-sensor validation approach of an end-effector-based robot for the rehabilitation of the upper and lower limb. *Electronics* **2020**, *9*, 1751. [CrossRef]
14. Tiboni, M.; Filippini, A.; Amici, C.; Vetturi, D. Test-Bench for the Characterization of Flexion Sensors Used in Biomechanics. *Electronics* **2021**, *10*, 2994. [CrossRef]
15. Takahashi, C.D.; Der-Yeghiaian, L.; Le, V.; Motiwala, R.R.; Cramer, S.C. Robot-based hand motor therapy after stroke. *Brain* **2008**, *131*, 425–437. [CrossRef]
16. Bayındır, O.; Akyüz, G.; Sekban, N. The effect of adding robot-assisted hand rehabilitation to conventional rehabilitation program following stroke: A randomized-controlled study. *Turk. J. Phys. Med. Rehabil.* **2022**, *68*, 254–261. [CrossRef]
17. Shi, X.Q.; Heung, H.L.; Tang, Z.Q.; Li, Z.; Tong, K.Y. Effects of a Soft Robotic Hand for Hand Rehabilitation in Chronic Stroke Survivors. *J. Stroke Cerebrovasc. Dis.* **2021**, *30*, 105812. [CrossRef]
18. Zhang, X.; Yue, Z.; Wang, J. Robotics in Lower-Limb Rehabilitation after Stroke. *Behav. Neurol.* **2017**, *2017*, 3731802. [CrossRef]
19. Tiboni, M.; Amici, C. Soft Gloves: A Review on Recent Developments in Actuation, Sensing, Control and Applications. *Actuators* **2022**, *11*, 232. [CrossRef]
20. Chu, C.Y.; Patterson, R.M. Soft robotic devices for hand rehabilitation and assistance: A narrative review. *J. Neuroeng. Rehabil.* **2018**, *15*, 9. [CrossRef] [PubMed]
21. Cheng, L.; Chen, M.; Li, Z. Design and Control of a Wearable Hand Rehabilitation Robot. *IEEE Access* **2018**, *6*, 74039–74050. [CrossRef]
22. Liu, C.; Lu, J.; Yang, H.; Guo, K. Current State of Robotics in Hand Rehabilitation after Stroke: A Systematic Review. *Appl. Sci.* **2022**, *12*, 4540. [CrossRef]
23. Rostami, H.R.; Arefi, A.; Tabatabaei, S. Effect of mirror therapy on hand function in patients with hand orthopaedic injuries: A randomized controlled trial. *Disabil. Rehabil.* **2013**, *35*, 1647–1651. [CrossRef]

24. Camp, A.S.; Chapman, E.M.; Cienfuegos, P.J. Modeling and analysis of hydraulic piston actuation of McKibben fluidic artificial muscles for hand rehabilitation. *Int. J. Robot. Res.* **2021**, *40*, 136–147. [CrossRef]

25. Copaci, D.S.; Blanco, D.; Martin-Clemente, A.; Moreno, L. Flexible shape memory alloy actuators for soft robotics: Modelling and control. *Int. J. Adv. Robot. Syst.* **2020**, *17*. [CrossRef]

26. Yurkewich, A.; Kozak, I.; Ivanovic, A.; Rossos, D.; Wang, R.; Hebert, D.; Mihailidis, A. Myoelectric untethered robotic glove enhances hand function and performance on daily living tasks after stroke. *J. Rehabil. Assist. Technol. Eng.* **2020**, *7* . [CrossRef]

27. Tan, N.; Gu, X.; Ren, H. Design, characterization and applications of a novel soft actuator driven by flexible shafts. *Mech. Mach. Theory* **2018**, *122*, 197–218. [CrossRef]

28. Ebrahimi, N.; Jafari, A. Energy and Force Optimization of a Network of Novel Electromagnetic Soft Actuators. *Energies* **2020**, *13*, 3572. [CrossRef]

29. Manns, M.; Morales, J.; Frohn, P. Additive manufacturing of silicon based PneuNets as soft robotic actuators. *Procedia Cirp* **2018**, *72*, 328–333. [CrossRef]

30. Coyle, S.; Majidi, C.; LeDuc, P.; Hsia, K.J. Bio-inspired soft robotics: Material selection, actuation, and design. *Extrem. Mech. Lett.* **2018**, *22*, 51–59. [CrossRef]

31. Rad, C.; Hancu, O.; Lapusan, C. Data-Driven Kinematic Model of PneuNets Bending Actuators for Soft Grasping Tasks. *Actuators* **2022**, *11*, 58. [CrossRef]

32. Polygerinos, P.; Lyne, S.; Wang, Z.; Nicolini, L.; Mosadegh, B.; Whitesides, G.; Walsh, C. Towards a soft pneumatic glove for hand rehabilitation. In Proceedings of the 2013 IEEE/RSJ International Conference on Intelligent Robots and Systems, Tokyo, Japan, 3–7 November 2013; pp. 1512–1517. [CrossRef]

33. Stano, G.; Arleo, L.; Percoco, G. Additive Manufacturing for Soft Robotics: Design and Fabrication of Airtight, Monolithic Bending PneuNets with Embedded Air Connectors. *Micromachines* **2020**, *11*, 485. [CrossRef]

34. Jiang, Y.; Chen, D.; Que, J.; Liu, Z.; Wang, Z.; Xu, Y. Soft Robotic Glove for Hand Rehabilitation Based on a Novel Fabrication Method. In Proceedings of the IEEE International Conference on Robotics and Biomimetics (ROBIO), Macau, Macao, 5–8 December 2017. [CrossRef]

35. Bhat, A.; Yeow, R.C.H. Utilizing Sacrificial Molding for Embedding Motion Controlling Endostructures in Soft Pneumatic Actuators. In Proceedings of the IEEE/RSJ International Conference on Intelligent Robots and Systems (IROS), Las Vegas, NV, USA, 24 October 2020–24 January 2020. [CrossRef]

36. Mosadegh, B.; Polygerinos, P.; Keplinger, C.; Wennstedt, S.; Shepherd, R.F.; Gupta, U.; Shim, J.; Bertoldi, K.; Walsh, C.J.; Whitesides, G.M. Pneumatic Networks for Soft Robotics that Actuate Rapidly. *Adv. Funct. Mater.* **2014**, *24*, 2163–2170. [CrossRef]

37. Marechal, L.; Balland, P.; Lindenroth, L.; Petrou, F.; Kontovounisios, C.; Bello, F. Toward a Common Framework and Database of Materials for Soft Robotics. *Soft Robot.* **2021**, *8*, 284–297. [CrossRef]

38. López-Campos, J.A.; Segade, A.; Casarejos, E.; Fernández, J.R.; Días, G.R. Hyperelastic characterization oriented to finite element applications using genetic algorithms. *Adv. Eng. Softw.* **2019**, *133*, 52–59. [CrossRef]

39. Matheus, S.X.; Fleming, A.J.; Yong, Y.K. Finite Element Modeling of Soft Fluidic Actuators: Overview and Recent Developments. *Adv. Intell. Syst.* **2020**, *3*, 2000187. [CrossRef]

40. Al-Sharadqah, A.; Chernov, N. Error analysis for circle fitting algorithms. *Electron. J. Stat.* **2009**, *3*, 886–911. [CrossRef]

41. Wick-Joliat, R.; Tschamper, M.; Kontic, R.; Penner, D. Water-soluble sacrificial 3D printed molds for fast prototyping in ceramic injection molding. *Addit. Manuf.* **2021**, *48*, 102408. [CrossRef]

42. Low, J.H.; Goh, J.Y.; Cheng, N.; Khin, P.M.; Han, Q.Q.; Yeow, C.H. A Bidirectional 3D-printed Soft Pneumatic Actuator and Graphite-based Flex Sensor for Versatile Grasping. In Proceedings of the 2020 IEEE International Conference on Robotics and Automation (ICRA), Paris, France, 31 May–31 August 2020; pp. 7979–7985. [CrossRef]

43. Xingchen, C.; Zhezhi, L.; Bing, Z.; Xiaoduo, T.; Fuqiang, F.; Yu, F.; Junhu, Z.; Tieqiang, W.; Fanbao, M. Sponge-like, semi-interpenetrating self-sensory hydrogel for smart photothermal-responsive soft actuator with biomimetic self-diagnostic intelligence. *Chem. Eng. J.* **2023**, *467*, 143515. [CrossRef]

44. Luo, Y.; Abidian, M.R.; Ahn, J.h.; Akinwande, D.; Andrews, A.M.; Antonietti, M.; Bao, Z.; Berggren, M.; Berkey, C.A.; Bettinger, C.J.; et al. Technology Roadmap for Flexible Sensors. *ACS Nano* **2023**, *17*, 5211–5295. [CrossRef] [PubMed]

45. Tiboni, M.; Remino, C. Condition monitoring of a mechanical indexing system with artificial neural networks. In Proceedings of the WCCM 2017—1st World Congress on Condition Monitoring 2017, London, UK, 13–16 June 2017.

46. Tiboni, M.; Incerti, G.; Remino, C.; Lancini, M. Comparison of signal processing techniques for condition monitoring based on artificial neural networks. *Appl. Cond. Monit.* **2019**, *15*, 179–188. [CrossRef]